International Journal of Precision Engineering and Manufacturing (2019) 20:963–972
https://doi.org/10.1007/s12541-019-00114-z

Online ISSN 2005-4602
Print ISSN 2234-7593

REGULAR PAPER

A Comparative Study of Non-destructive Evaluation of Glass Fiber Reinforced Polymer Composites Using Terahertz, X-ray, and Ultrasound Imaging

Jie Wang[1] · Jin Zhang[1] · Tianying Chang[1,2] · Hong-Liang Cui[1,3]

Received: 30 September 2018 / Revised: 20 March 2019 / Accepted: 24 March 2019 / Published online: 16 April 2019

Abstract

A set of samples of glass fiber reinforced polymer composites with Teflon inclusions in the shape of pentagram have been specifically designed and fabricated for the purpose of assessing the efficacy and practicality of terahertz (THz) time domain spectroscopy (TDS) system in non-destructive evaluation (NDE), in side-by-side comparison with X-ray computed tomography (CT), and ultrasonic imaging. The samples feature systematic variation of Teflon inclusions of a variety of thicknesses and placement depths. An improved THz imaging algorithm is proposed and demonstrated to enhance the capability of THz-TDS detection by adding an appropriate window for sampling the reflected time-domain waveform a posteriori. Additionally, image fusion algorithm based on block segmentation is applied to combine multiple imaging detection results, leading to further improvement of the final defect detection capability. Comparative analysis of the detection results among THz-TDS, X-ray CT, and ultrasonic imaging is carefully carried out to assess the merits and disadvantages of each technique, and to attempt to find a proper place for THz-TDS imaging in the traditional arsenal of NDE tools.

Keywords Glass fiber reinforced polymer composites · Terahertz · X-ray · Ultrasound · Window-based image processing · Image fusion

List of Symbols

- d Thickness of the sample
- c The THz wave propagation speed in air
- n_s The refractive index of the sample
- Δt The time delay difference

1 Introduction

Glass fiber reinforced polymer (GFRP) composites have been widely used in aerospace, transportation, building and other related industries due to their light weight, high specific strength, strong corrosion resistance, and excellent thermal and acoustic insulation power [1]. However, various defects may be introduced in GFRP composites during their manufacturing and serving processes, such as foreign inclusions, voids, delamination, mechanical and thermal damages [2]. Therefore, non-destructive evaluation (NDE) technologies are required to detect the defects, to ensure the quality of GFRP composites.

A multitude of NDE technologies capable of detecting GFRP composites have been developed over the years. Among them, X-ray computed tomography (CT) [3, 4] and ultrasonic imaging technologies [5, 6] are the most prevalent. However, both of them have their own strengths and weaknesses. X-ray CT can provide clear images of internal features and locate the depth with high resolution, but this method has ionizing radiation, which is harmful to the human body [7]. The ultrasound method has good processing speed and strong penetrating power, but lateral and axial spatial resolution are limited; and liquid coupling is required, which may contaminate the sample [8]. THz-TDS technology is a non-contact detection modality, can provide non-ionizing examination for non-polar and non-conductive materials, and has in recent years demonstrated great

✉ Jin Zhang
zhangjin0109@jlu.edu

[1] College of Instrumentation and Electrical Engineering, Jilin University, Changchun 130061, Jilin, China

[2] Institute of Automation, Qilu University of Technology (Shandong Academy of Sciences), Jinan 250014, Shandong, China

[3] Chongqing Institute of Green and Intelligent Technology, Chinese Academy of Sciences, Chongqing 400714, China

potential in becoming a useful complement of the traditional NDE methods [9–14].

A number of investigations have been reported regarding NDE of GFRP composites using THz-TDS technology. Rutz et al. [15] examined fiber directions of GFRP composites by using THz-TDS. Stoik et al. [16, 17] used transmitted and reflected THz-TDS to detect the defects of aircraft composites such as burn damage, bending damage and internal holes. Ospald et al. [18] tested impact damage, foreign inclusion, debonding, delamination and porosity of glass fiber composites by using reflected THz-TDS. Dong et al. [19] used reflected THz-TDS to detect GFRP composites with forced delamination and removed the effect of water vapor by wavelet denoising. Ryu et al. [20] investigated GFRP composite with multi-delamination defects using THz-TDS. Zhang et al. [21] employed THz-TDS in reflected and transmitted modes to detect the Teflon inclusions of two types of GFRP laminates (epoxy GFRP composites and polyester GFRP composites). Kim et al. [22] used THz-TDS to analyze the effects of reflection, scattering and absorption of THz radiations with respect to the type of hidden damages (delamination, fiber fracture and moisture absorption). Further, both the transmission and reflection configurations were successfully used to image the hidden damages. Although THz technology has achieved some enviable results for defect detection, THz imaging still has many obstacles, such as low resolution and imperfect image processing algorithms. Therefore, improving THz imaging algorithm and image processing remains an interesting and important research topic. In this study, we have improved the traditional THz imaging algorithm in the reflection mode, and put forth a novel segmented THz imaging treatment based on a windowed approach for the reflected time-domain waveforms. Moreover, we have introduced an image fusion algorithm based on block segmentation to combine relevant defect information from two or more detected images into a single image to improve its quality.

In recent years several research groups have studied and compared the detection capability of THz, X-ray, and/or ultrasound imaging for GFRP composites. Dong et al. [8] examined GFRP composites with forced delamination defects using THz-TDS and ultrasound imaging. Matheis et al. [23] employed THz frequency modulated continuous wave, X-ray, and ultrasound imaging to inspect GFRP composites with multiple forced delamination defects, and obtained their defect detection rates. Yang et al. [24] used THz, X-ray, and ultrasound imaging to examine wind turbine blade composites with fiber breakage defects, and reached certain conclusions regarding strengths and limitations of NDT techniques through comparison studies. However, to date THz-TDS, X-ray and ultrasonic imaging have not been employed simultaneously to quantitatively measure depths and thicknesses of irregular inclusions hidden in GFRP composites. In this paper, we systematically carry out THz-TDS, X-ray CT and ultrasound imaging to detect GFRP composites, using a group of samples that are inserted Teflon inclusions with different thicknesses and depths in the shape of pentagram. The results of these three NDE techniques have provided a complete set of useful data for a careful comparison and discussion.

The remainder of the paper is organized as follows. Section 2 serves to introduce the THz-TDS system and the experimental setup, as well as to describe the preparation of samples and their specifications. Image algorithms are introduced in Sect. 3; THz-TDS measurements and results are discussed in Sect. 4, while Sect. 5 is devoted to the comparison of imaging procedure and results with X-ray CT and ultrasonic imaging. Finally, summary and conclusion are contained in Sect. 6.

2 THz Imaging System and Sample Preparation

2.1 THz System

The FICO THz-TDS system from Zomega is employed in this study, as shown schematically in Fig. 1. The time domain range is from 0 to 100 ps with 0.05 ps resolution, and the effective spectral measure range is from 0.1 to 2 THz with 11 GHz resolution. The minimum scanning step of two-dimensional (both vertical and horizontal directions) platform is 0.05 mm, and the maximum scanning area is 150×150 mm^2. The THz-TDS system has two working modes: transmission mode and reflection mode. In the process of sample test, the whole system is in a sealed chamber filled with dry air.

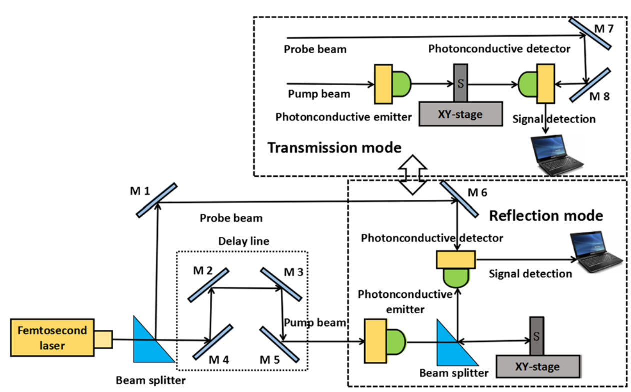

Fig. 1 Schematic diagram of THz-TDS system in both reflection and transmission modes (M1–M8: mirrors)

2.2 Preparation of Samples

In this paper, the experimental samples are epoxy GFRP composites, which consist of multilayer glass fiber cloths and epoxy resin adhesive, through a laminating process. A single-ply glass fiber cloth is about 0.2 mm thick. The size of all samples is 100 mm × 100 mm × 3 mm. Two kinds of Teflon inclusions are investigated in this paper. The first GFRP sample (Sample-1) is inserted four Teflon films with different thicknesses at the same depth (between the seventh and eighth layers). The Teflon films with thicknesses of about 0.47 mm, 0.22 mm, 0.12 mm and 0.08 mm are labeled defect 1, defect 2, defect 3 and defect 4, respectively. A three-dimensional rendering of Sample-1 is shown in Fig. 2a. The second GFRP sample (Sample-2) is inserted six Teflon films with the same thickness (0.1 mm) at different depths. The labels and depths of the Teflon films inserted in Sample-2 are shown in Table 1. A three-dimensional rendering of Sample-2 is shown in Fig. 2b. All the Teflon films are in the shape of pentagram with the same area. The diameter of the pentagram is 20 mm, and the sharp angle is 36°, as shown in Fig. 2c.

3 Imaging Algorithms

3.1 Traditional THz Imaging Algorithm

THz-TDS system scans sample in the horizontal and vertical directions, collecting the time domain waveform for each space point of the sample. We can build up two kinds of two-dimensional imaging, commonly referred to as C-scan imaging and B-scan imaging [25, 26]. For a C-scan image, the abscissa and ordinate values represent the horizontal and vertical positions of the sample, respectively. THz C-scan imaging can be divided into time domain and frequency domain imaging. Time domain image uses specific information of the time domain waveform, such as electric field amplitude maximum, minimum, peak-to-peak, and intensity, etc. Frequency domain imaging uses specific information of the frequency domain waveform, such as amplitude, power spectral density, energy, and phase at certain frequency. For different defects, we can select different imaging algorithm to achieve the best imaging effect. For B-scan imaging, the abscissa values represent the horizontal or vertical positions of the sample, and the ordinate values represent the time delay (equivalent to depth into the sample). Each column contains an entire THz time domain waveform of a spatial point of the sample, showing the depth information of the sample.

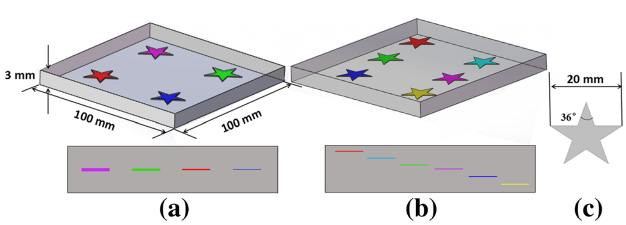

Fig. 2 Defect configuration of the GFRP composites: three-dimensional rendering of samples, and thicknesses and depths information of inclusions in cross section of samples: **a** Sample-1: purple, green, red and dark blue correspond to defect 1, defect 2, defect 3 and defect 4, respectively; **b** Sample-2: red, light blue, green, purple, dark blue and yellow correspond to defect 1, defect 2, defect 3, defect 4, defect 5 and defect 6, respectively; **c** star-shaped defect. (Color figure online)

3.2 An Improved THz Imaging Algorithm

In this paper, we propose and demonstrate a new processing algorithm for reflected THz C-scan imaging. The traditional reflected THz C-scan imaging shows the whole information of the sample, including both sample surface and internal structure. Because the reflected pulse from the surface of sample is ordinarily much stronger than that from inside defects, the sample surface information always overwhelms the inside information of the sample. Therefore, it is necessary to put forward a new processing algorithm to inspect the hidden defects. First, we analyze the whole reflected time domain waveforms, determine the position of the reflected pulses from the front surface of the sample, and then perform the THz C-scan imaging after removing the reflected pulses from the front surface of the sample. Second, we perform the THz B-scan imaging on the defect area of the THz C-scan image obtained in the previous step. Third, we extract the reflected time domain waveforms of the sample with and without defects. A threshold value is set for peak detection, which is performed on the reflected time domain waveforms between the reflected pulses from the front and rear surfaces of the sample. The detected peaks are usually caused by the defects hidden inside the sample. Fourth, combining the THz B-scan images and the detected peaks, we can determine the number and position of the reflected pulses from the defects in the reflection time domain waveforms. According to the analyzing results of the defects, we introduce appropriate time windows to the

Table 1 Depths of Teflon inclusions in Sample-2

Defect No	1	2	3	4	5	6
Defect depth	Between layer 3 and 4	Between layer 5 and 6	Between layer 7 and 8	Between layer 9 and 10	Between layer 11 and 12	Between layer 13 and 14

reflected time domain waveforms, and several time periods are obtained. Every time period contains different depth information of the sample. Fifth, the THz C-scan imaging is performed for every time period, and the defects at different depths are imaged separately. Finally, an image fusion method is used to combine the multiple THz C-scan images obtained through different time periods, and all the hidden defects can be shown in a new fused image. In this paper, an image fusion algorithm based on wavelet decomposition is adopted [27]. The original image is decomposed with three-scale, and sym3 is used as the wavelet basis. In order to achieve ideal fusion effect, the image fusion algorithm based on the block segment is selected in the experiments. For Sample-2, we segment every detection image into six blocks, and then make the corresponding block with the same location to fuse.

4 THz Measurement Results

In both the transmission and reflection mode, the scanning step size is set at 1 mm, and the scanning area at $100 \times 100\ mm^2$.

4.1 Measurement of Sample-1

Figure 3 shows the THz C-scan imaging results of Sample-1. Figure 3a, b are separately the transmitted and reflected amplitude images at 0.18 THz obtained through the traditional imaging algorithm, and the Fourier transform is carried out for the entire time domain waveform. From Fig. 3a, b, we can see that the Teflon inclusions with different thicknesses are significantly different in the THz image. In both the transmission and reflection mode, when the Teflon inclusion is thicker, the difference of the gray value between the defect area and non-defect area is bigger. Hence, we can conclude that the thickness of the inclusion has significant impact on the ability of the THz wave to detect the inclusion, and it is easier to detect the thicker inclusions. Figure 3c is the reflected amplitude image at 0.18 THz, which removes the reflected THz pulse from the front surface of the sample, whose time delay is smaller than 30 ps. By comparison between Fig. 3b, c, the imaging effect of the inclusions is slightly improved. Figure 4 shows the reflected THz B-scan imaging results, corresponding to the vertical red dashed lines in Fig. 3c. From Fig. 4, we can see that four inclusions with different thicknesses are almost at the same depth. However, as can be seen from Fig. 4a, the defect 1 is not flat, which is thick in the middle and thin on both sides. From Fig. 3a–c, we cannot detect the abnormal phenomenon. Figure 5 shows the whole reflected time domain waveforms measured on the Sample-1 with and without defects, and the color of the waveforms corresponds to that of the rhombuses in Fig. 3b, which mark the locations of the waveform acquisition. The reflected THz pulses at about 89 ps are from the system optics, and can be neglected. The reflected THz pulses at about 22 ps are caused by the front surface of Sample-1, and the reflected THz pulses at about 66 ps are resulted from the rear surface of Sample-1. In order to eliminate the influence of the small reflected pulses from glass fiber cloth, we set a threshold value for peak detection. Here, the reflected pulses whose

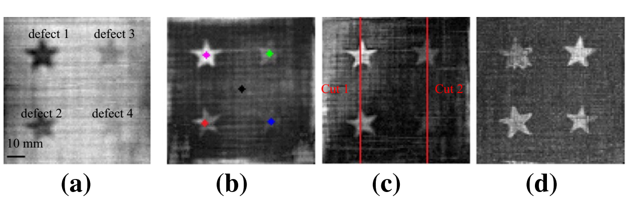

Fig. 3 THz C-scan imaging results of Sample-1: **a** transmitted, and **b** reflected amplitude image at 0.18 THz with the traditional THz imaging algorithm; **c** reflected amplitude image at 0.18 THz, with the reflection from the front surface removed before imaging processing; **d** time domain maximum peak imaging with the new THz imaging algorithm

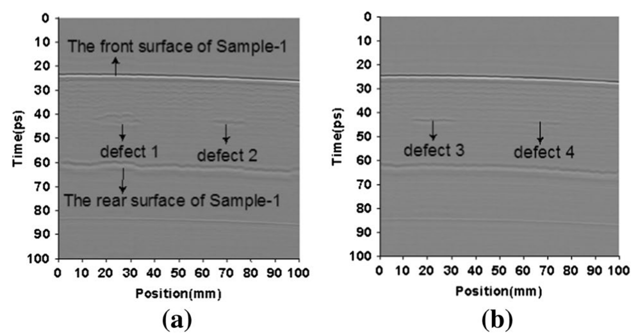

Fig. 4 Reflected THz B-scan imaging results of Sample-1: **a** Cut 1, and **b** Cut 2 column, corresponding to the vertical red dashed lines in Fig. 3c, respectively . (Color figure online)

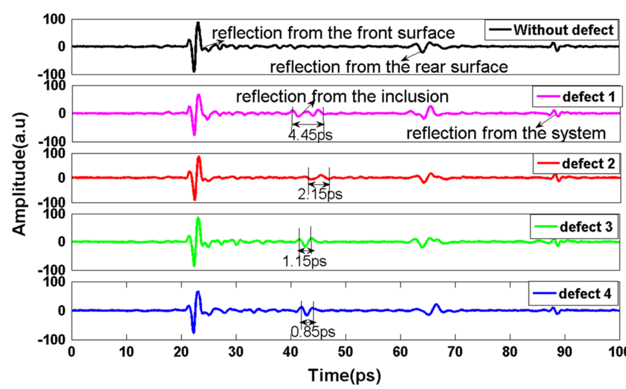

Fig. 5 Reflected THz time domain waveforms measured from Sample-1, corresponding to the colored pixel dots in Fig. 3b . (Color figure online)

peak values are greater than 8 are considered to be from the Teflon inclusions. Based on the results of peak detection and THz B-scan imaging, a window with the center at 42 ps and a width of 10 ps is added, and the reflected time domain waveform from 37 to 47 ps is acquired. As we can see, the reflected pulses from Teflon inclusions at 37–47 ps have different forms. The polarity of the reflected THz pulse is associated with the refractive index change at an interface. For reflection from a low refractive index medium to a high refractive index medium, the reflected pulse changes polarity. For reflection from a high refractive index medium to a low refractive index medium, the reflected pulse's polarity is unchanged. When the inclusion is very thin, the reflections from the front and rear surfaces of the Teflon inclusion may be overlapped to a certain degree. Figure 3d is the time domain maximum peak imaging with time delay between 37 and 47 ps. From Fig. 3d, we can see that all the Teflon inclusions can be detected, including that with minimum thickness, and all the angles of the pentagrams are shown much more clearly than those detected by the traditional THz imaging algorithm (Fig. 3a–c). Furthermore, the abnormal phenomenon of defect 1 can also be detected. In combination with Fig. 4a, we can infer that the inclusion of defect 1 may be distorted in the axial direction during the laminating process. The thicknesses of the Teflon inclusions can be obtained through the time-of-flight relation:

$$d = \frac{c\Delta t}{2n_s} \tag{1}$$

where d is the thickness of the sample, c is the THz wave propagation speed in air, n_s is the refractive index of the sample, and Δt is the time delay difference. The published refractive index of the Teflon is 1.5 [21]. From Fig. 4, the time delay differences of the reflected pulses between the front and rear surfaces of the sample for the four Teflon inclusions are 4.45 ps, 2.15 ps, 1.15 ps, and 0.85 ps, respectively. By Eq. (1), we can calculate the thicknesses of Teflon inclusions are 0.455 mm, 0.215 mm, 0.115 mm, and 0.085 mm, respectively, which is noted as Tt shown in Table 2.

4.2 THz Measurement of Sample-2

Figure 6 shows the THz C-scan imaging results of the Sample-2. Figure 6a, b are separately the transmitted and reflected amplitude images at 0.2 THz obtained through the traditional imaging algorithm. From Fig. 6a, b, we can see that the Teflon inclusions with different insertion depths have almost the same imaging effects. Therefore, we can conclude that when the energy of the THz wave is strong enough, the THz wave has the same ability to detect the inclusions with different insertion depths in both the transmission and reflection modes. Figure 6c is the reflected amplitude image at 0.2 THz, which removes the reflected THz pulse from the front surface of the sample, whose time delay is smaller than 25 ps. By comparison between Fig. 6b, c, the imaging effect of the inclusions is slightly improved. To display the relative depths of the Teflon inclusions intuitively, THz B-scan imaging is performed, as shown in Fig. 7, corresponding to the vertical red dashed lines in Fig. 6c, respectively. From Fig. 7, the six Teflon inclusions with the same thickness at different depths can be seen clearly. Figure 8 shows the reflected time domain waveforms from the different Teflon inclusions in Sample-2. The color of the waveforms corresponds to that of the rhombuses in Fig. 6b, which mark the locations of the waveform acquisition. From Fig. 8, we can find that the amplitude of the reflected pulses from the Teflon inclusions become smaller, as the insertion depth of the Teflon inclusions increases, due to THz wave attenuation during the propagation process. Here, the reflected pulses whose peak values are greater than 8 are considered to be from the Teflon inclusions. Based on the B-scan imaging of Fig. 7 and the peak detection results of Fig. 8, six sliding windows with 4 ps width are introduced, with the centers of the windows at the peak positions of the reflection pulses form the Teflon inclusions (31 ps, 36 ps,

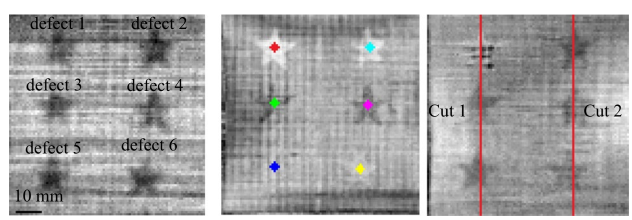

Fig. 6 THz C-scan imaging results of Sample-2: **a** transmitted, and **b** reflected amplitude image at 0.20 THz with the traditional THz imaging algorithm; **c** reflected amplitude image at 0.20 THz, with the reflection from the front surface removed before imaging processing

Table 2 Measured thicknesses and depths of Teflon inclusions

Defect No Sample-1 (Teflon thickness)	1	2	3	4	Defect No Sample-2 (Teflon depth)	1	2	3	4	5	6
Tt (mm)	0.455	0.215	0.115	0.085	Dt (mm)	0.508	0.872	1.255	1.638	1.950	2.327
Tx (mm)	0.470	0.220	0.120	0.080	Dx (mm)	0.500	0.850	1.340	1.750	2.060	2.430
					Du (mm)			1.200	1.500	1.900	2.300

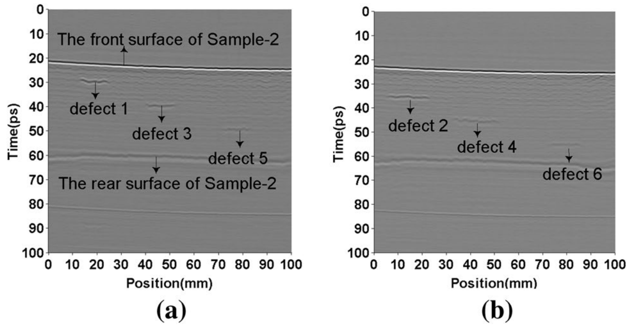

Fig. 7 Reflected THz B-scan imaging results of Sample-2: **a** Cut 1 and **b** Cut 2 column, corresponding to the vertical red dashed lines in Fig. 6c, respectively . (Color figure online)

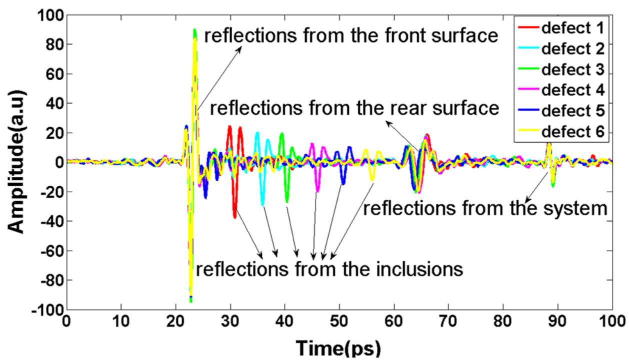

Fig. 8 Reflected THz time domain waveforms measured on Sample-2, corresponding to the colored pixel dots in Fig. 6b, respectively

41 ps, 46 ps, 51 ps and 56 ps). Hence, six time periods are obtained, which are 29–33 ps, 34–38 ps, 39–43 ps, 44–48 ps, 49–53 ps, and 54–58 ps respectively. Figure 9a–f take the time domain maximum peak imaging based on the above six time periods separately, and each image detects a corresponding Teflon inclusion exclusively. Figure 9g is the fused image for Fig. 9a–f, and all six Teflon inclusions can be seen clearly in the single fused image. The fusion rule of the low frequency subband adopted in the present case is selecting the maximum value of the low frequency coefficients for all block images, and the fusion rule of the high frequency subband is calculating a weighted average for all block images. In our previous work, the refractive index of epoxy GFRP composites has been calculated, whose value was found to be 2.1 [16]. From Fig. 8, we obtain the time delay differences between the Teflon inclusions and the front surface of the sample as 7.12 ps, 12.21 ps, 17.57 ps, 22.93 ps, 27.30 ps, and 32.57 ps, respectively. According to Eq. (1), we can calculate the depths of the six Teflon inclusions are 0.508 mm, 0.872 mm, 1.255 mm, 1.638 mm, 1.950 mm, and 2.327 mm, respectively, which are entered as values for Dt in Table 2.

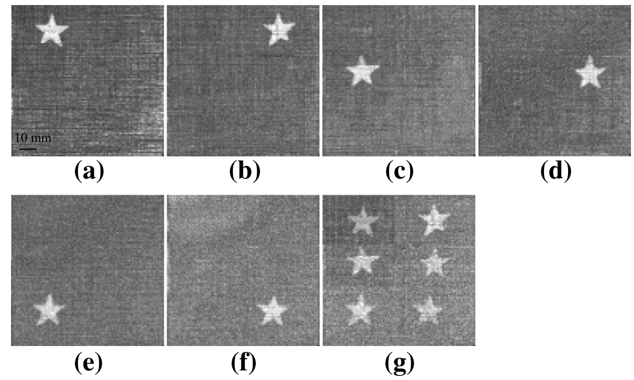

Fig. 9 Reflected THz C-scan imaging results of Sample-2 with the new THz imaging algorithm: the time domain maximum peak imaging for the time periods of **a** 29–33 ps, **b** 34–38 ps, **c** 39–43 ps, **d** 44–48 ps, **e** 49–53 ps and **f** 54–58 ps; **g** fused image for **a**–**f**

5 Comparison with X-ray CT and Ultrasonic Measurement Results

5.1 X-ray CT Measurement Results

The same samples are investigated using an X-ray CT imaging system. The micro focus radiation source is FXE-225 kV tube manufactured by YXLON. In this work, the tube voltage is 70 kV and the tube current intensity is 1.5 mA. The sample is mounted on a platform, which is 380 mm from the radiation source. The voxel size is 1 mm × 1 mm × 0.05 mm in this work. The rotating and rising platform has an angle of 30° with the radiation source, whose rotating step is 0.5°. All experiments in this section select a cone beam scanning, and the X-ray CT image is reconstructed. VG Studio Max 3.0 software is used to process and analyze the X-ray CT image.

Figure 10 shows two of the CT image slices of Sample-1 at different depth in the axial direction. From Fig. 10a, we can see that the four Teflon inclusions are barely detected, and the images are basically consistent with the THz detection results. As can be seen from the red ellipse of Fig. 10b, the sharp angle of the pentagram shifted in the lower right corner, which confirms the THz detection results that the defect 1 is distorted in the axial direction. Figure 11a–f show six of CT image slices of Sample-2 at different depths in the axial direction, and each image slice shows a Teflon inclusion. With the help of the image fusion algorithm, all the inclusion defects are finally shown in a new image. The fusion rule of both the low frequency subband and high frequency subband adopted in the present case is selecting the minimum value of the low frequency coefficients for all block images.

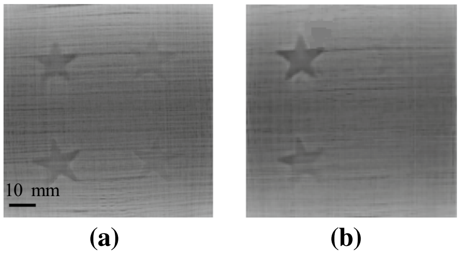

Fig. 10 X-ray CT image slices of the Sample-1 at different depths in the axial direction: **a** depth 1.32 mm, and **b** depth 1.42 mm

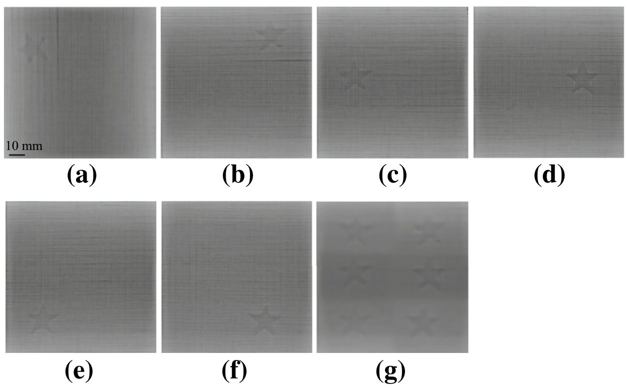

Fig. 11 X-ray CT image slices of Sample-2 at **a** depth 0.50 mm, **b** depth 0.85 mm, **c** depth 1.34 mm, **d** depth 1.75 mm, **e** depth 2.06 mm, and **f** depth 2.43 mm in the axial direction; **g** fused image for **a**–**f**

5.2 Ultrasonic Measurement Results

The samples are also investigated using a reflected ultrasonic C-scan imaging system. With an eye on the competing demands of power/attenuation and resolution, we compromise by selecting the focused-immersion transducer with a central frequency of 15 MHz to detect the GFRP composites. Reflected ultrasonic C-scan imaging system is performed on the samples with water coupling, hence, the sample should be waterproof. The ultrasonic scanning step size is 1 mm and scanning area is 100×100 mm^2. To provide sharper contrast reflected ultrasonic C-scan images, we choose different windowed time slice in the waveform to display inside information of samples in the form of C-scan imaging.

Figure 12a shows the reflected ultrasonic C-scan imaging result of Sample-1. The center and width of the window used in Fig. 12a is 1.3 μs and 0.5 μs, respectively. For the inclusion of defect 1, the angles of the pentagram can hardly be seen and the abnormal phenomenon in axial direction cannot be detected. Moreover, the defect 4 with minimum thickness can barely be detected. The reflected ultrasonic C-scan imaging results of Sample-2 are shown in Fig. 12b, c. Figure 12b, c are built up with the different windowed reflected ultrasonic waveforms separately. The center and width of the window used in Fig. 12b are 0.75 μs and 1.5 μs, respectively, and the center and width of the window used in Fig. 12c are 1.85 μs and 1.5 μs, respectively. The inclusions of defect 1 to defect 4 are detected in Fig. 12b, whereas the inclusions of defect 3 to defect 6 are detected in Fig. 12c. Figure 12d is the image fusion result of Fig. 12b, c, and all the inclusions can be seen in the new fused image. The fusion rule of both the low frequency subband and high frequency subband adopted in the present case is selecting the minimum value of the low frequency coefficients for all block images.

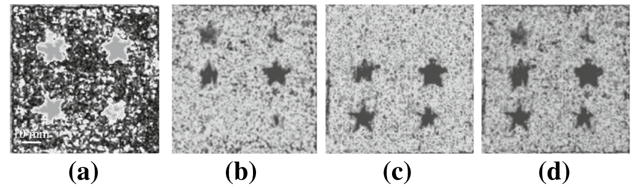

Fig. 12 Reflected ultrasonic C-scan imaging results: **a** Sample-1, **b** and **c** Sample-2, based on different windowed reflected ultrasonic waveforms separately; **d** fused image for Fig. 11b, c

5.3 Comparison with X-ray CT and Ultrasonic Measurement Results

For all three NDE technologies of THz-TDS, X-ray CT and ultrasonic imaging, the detection ability deteriorates as the Teflon inclusion becomes thinner, while the inclusion insertion depth has little impact on the quality of imaging. Comparison among THz-TDS, X-ray CT and ultrasonic imaging can be performed with respect to spatial resolution, which contains two parts, lateral and axial resolution.

Lateral resolution is the minimum distance that can be distinguished between two diffraction points across the scan plane. For THz-TDS and ultrasonic imaging, the lateral resolution is related to the diffraction-limited spot size of the beam, which varies with frequency. When the frequency is higher, the spot size is smaller, and the lateral resolution is higher. In our THz-TDS system, the lateral resolution is about 0.366–3.66 mm at 0.1–1 THz. The THz time domain imaging is a comprehensive reflection of the influence of all the frequency components, and its resolution is between the high frequency and low frequency limits. In our ultrasonic system, the lateral resolution is 1.1 mm for the focused-immersion transducer at 15 MHz. For X-ray CT imaging, the lateral resolution is related to the voxel size. When the voxel is smaller, the resolution is higher. In our X-ray CT system, the lateral resolution can reach 6 μm. Therefore, in theory, X-ray CT imaging can achieve the highest lateral resolution than the other two, and THz-TDS imaging has a higher resolution than ultrasonic imaging. Comparing the detection results of improved THz-TDS imaging (Figs. 3d, 9g), and X-ray CT imaging (Figs. 10a, 11g), although the lateral resolution of the THz-TDS imaging is lower than that of X-ray CT imaging, the detection effect of improved THz-TDS imaging for Teflon inclusion is obviously better than X-ray CT imaging on the whole. For X-ray CT imaging, Teflon inclusion can hardly be distinguished from the GFRP composites, which is because that the density of GFRP composites and Teflon is very similar, providing little contrast for X-ray radiation. Comparing the detection results of improved THz-TDS imaging (Figs. 3d, 9g) and ultrasonic imaging (Fig. 12a, d), we can see that the improved THz-TDS imaging for Teflon inclusion has obviously much better resolution than ultrasonic imaging.

Axial resolution is the minimum distance that can be distinguished between two points in depth. For THz-TDS and ultrasonic system, the axial resolution is equal to half the spatial pulse length, and it is high when the spatial pulse length is short. In our THz-TDS system, the axial resolution d can be calculated through Eq. (1), where Δt would be the half width of the THz pulse (1 ps). The axial resolution in our THz-TDS system is estimated to be about 70 μm. In our ultrasonic system, the axial resolution is 123 μm. For X-ray CT system, the axial resolution is determined by the height of the voxel size. When the height of voxel size is smaller, the axial resolution is higher. In our X-ray CT system, the axial resolution can reach 6 μm. In theory, X-ray CT system has the best axial resolution. Therefore, we measure the thicknesses and depths of the inclusions by X-ray CT system, and take them as the nominal values (entries in Table 2). For ultrasonic system, due to the poor axial time resolution, the reflected pulses from the front and rear surface of Teflon inclusion are completely overlapped. Therefore, the ultrasonic detection cannot provide quantitative thickness information about Teflon inclusions. Based on the sound velocity of GFRP composites and the time delay difference between reflected pulses from the front surface of sample and inclusion, we can calculate the depths of inclusions by ultrasonic system and show them in Table 2. Because the reflected pulses from defect 1 and defect 2 overlap with the initial ultrasonic pulse, we cannot obtain their depths. In Table 2, Tt and Tx represent the thickness of the four Teflon inclusions inserted in Sample-1 measured by THz-TDS and X-ray CT, respectively. Dt, Dx, Du represent the depths of the six Teflon inclusions in Sample-2 measured by THz-TDS, X-ray CT, and ultrasound, respectively. By comparison between Tt and Tx, we calculate the standard deviation as ± 0.009. By comparison between Dt and Dx, the standard deviation is ± 0.08. By comparison between Du and Dx, the standard deviation is ± 0.18. Based on the above comparison analysis, it is apparent that THz-TDS performed on par with X-ray CT in detecting depths and thicknesses of Teflon inclusions, and could provide higher axial resolution for detecting depths and thicknesses of Teflon inclusions than ultrasound.

6 Summary and Conclusion

In this study, we have systematically carried out THz-TDS, X-ray CT and ultrasonic imaging of GFRP composites inserted with small-area Teflon films, having different thicknesses and depths, in the shape of pentagram to simulate buried defects. For the reflected THz-TDS imaging modality, a new window-based algorithm has been employed, and the defect detection effect has been improved drastically. In addition, the use of image fusion algorithm based on block segment ensures that all the defects detected based on the information of different time periods can be integrated into one high-quality composite image. Moreover, by comparing the detection results of THz-TDS, X-ray CT and ultrasonic imaging, it is demonstrated unambiguously that the proposed new THz imaging approach can provide higher contrast ratio than X-ray CT technology in detecting thin Teflon inclusions hidden in GFRP composites, and has much higher lateral and axial resolution than ultrasound technology. As such, the proposed THz imaging approach can be employed as an effective alternative to and/or useful complement for the traditional NDE methods when dealing with GFRP composites or similar materials.

Acknowledgements This work was supported by the Ministry of Science and Technology of China (2015CB755401), National Natural Science Foundation of China (61705120), Department of Science & Technology of the Shandong Province (2017GGX10124, 2017GGX10108), Youth Science Funds of Shandong Academy of Sciences (2017QN0015), and Innovation Program of Shandong Academy of Sciences.

References

1. Burgueño, R., Karbhari, V. M., Seible, F., & Kolozs, R. T. (2001). Experimental dynamic characterization of an FRP composite bridge superstructure assembly. *Composite Structures, 54*(4), 427–444.
2. Berry, M., & Johnson, J. (2016). Effect of cold temperatures on the behavior and ultimate capacity of GFRP-reinforced concrete beams. *Cold Regions Science and Technology, 136,* 9–16.
3. Schilling, P. J., Karedla, B. P. R., Tatiparthi, A. K., Verges, M. A., & Herrington, P. D. (2005). X-ray computed microtomography of internal damage in fiber reinforced polymer matrix composites. *Composites Science and Technology, 65*(14), 2071–2078.
4. Thi, T. B. N., Morioka, M., Yokoyama, A., Hamanaka, S., & Yamashita, K. (2015). Measurement of fiber orientation distribution in injection-molded short-glass-fiber composites using X-ray computed tomography. *Journal of Materials Processing Technology, 219,* 1–9.
5. Zhu, W., Rose, J. L., Barshinger, J. N., & Agarwal, V. S. (1998). Ultrasonic guided wave NDT for hidden corrosion detection. *Research in Nondestructive Evaluation, 10*(4), 205–225.
6. Liu, L. D., & Wu, X. (2014). Defect types and ultrasonic nondestructive testing for fiber-reinforced composites. In Yarlagadda, P., & Kim, Y. H. (Eds.), *Advanced materials research* (Vol. 834–836, pp. 233–236).

7. Palka, N., & Panowicz, R. (2016). Non-destructive evaluation of puncture region in polyethylene composite by terahertz and X-ray radiation. *Composites Part B*, *92,* 315–325.
8. Dong, J., Kim, B., Locquet, A., McKeon, P., Declercq, N., & Citrin, D. (2015). Nondestructive evaluation of forced delamination in glass fiber-reinforced composites by terahertz and ultrasonic waves. *Composites Part B*, *79,* 667–675.
9. Chady, T., & Lopato, P. (2010). Testing of glass-fiber reinforced composite materials using terahertz technique. *International Journal of Applied Electromagnetics & Mechanics*, *33*(33), 1599–1605.
10. Hsu, D. K., Lee, K. S., Park, J. W., Woo, Y. D., & Im, K. H. (2012). NDE inspection of terahertz waves in wind turbine composites. *International Journal of Precision Engineering and Manufacturing, 13*(7), 1183–1189.
11. Im, K. H., Lee, K. S., Yang, I. Y., Yang, Y. J., & Seo, Y. H. (2013). Advanced T-ray nondestructive evaluation of defects in FRP solid composites. *International Journal of Precision Engineering and Manufacturing, 14*(6), 1093–1098.
12. Park, J. W., Im, K. H., Yang, I. Y., Kim, S. K., & Kang, S. J. (2014). Terahertz radiation NDE of composite materials for wind turbine applications. *International Journal of Precision Engineering and Manufacturing, 15*(6), 1247–1254.
13. Zhang, J., Shi, C. C., Ma, Y. T., Han, X. H., Li, W., Chang, T. Y., et al. (2015). Spectroscopic study of terahertz reflection and transmission properties of carbon-fiber-reinforced plastic composites. *Optical Engineering, 54*(5), 54106.
14. Zhang, J., Li, W., Cui, H. L., Shi, C. C., Han, X. H., Ma, Y. T., et al. (2016). Nondestructive evaluation of carbon fiber reinforced polymer composites using reflective terahertz imaging. *Sensors, 16*(6), 875–887.
15. Rutz, F., & Koch, M. (2017). Terahertz quality control of polymeric products. *International Journal of Infrared and Millimeter Waves*, *27*(4), 547–556.
16. Stoik, C., Bohn, M., & Blackshire, J. (2008). Nondestructive evaluation of aircraft composites using transmissive terahertz time domain spectroscopy. *Optics Express, 16*(21), 17039–17051.
17. Stoik, C., Bohn, M., & Blackshire, J. (2010). Nondestructive evaluation of aircraft composites using reflective terahertz time domain spectroscopy. *NDT and E International, 43*(2), 106–115.
18. Ospald, F., Zouaghi, W., Beigang, R. & Matheis, C. (2013). Aeronautics Composite Material Inspection with a Terahertz Time-domain Spectroscopy System. *Optical Engineering*, *53*, 031208.
19. Dong, J. L., Locquet, A., & Citrin, D. S. (2016). Enhanced terahertz imaging of small forced delamination in woven glass fibre-reinforced composites with wavelet de-noising. *Journal of Infrared, Millimeter, and Terahertz Waves, 37*(3), 289–301.
20. Ryu, C. H., Park, S. H., Kim, D. H., Jhang, K. Y., & Kim, H. S. (2016). Nondestructive evaluation of hidden multi-delamination in a glass-fiber-reinforced plastic composite using terahertz spectroscopy. *Composite Structures, 156,* 338–347.
21. Zhang, J., Wang, J., Han, X. H., & Cui, H. L. (2016). Noncontact detection of teflon inclusions in glass-fiber-reinforced polymer composites using terahertz imaging. *Applied Optics, 55*(36), 10215–10222.
22. Kim, D. H., Ryu, C. H., Park, S. H., & Kim, H. S. (2017). Nondestructive evaluation of hidden damages in glass fiber reinforced plastic by using the terahertz spectroscopy. *International Journal of Precision Engineering and Manufacturing-Green Technology, 2*(2), 211–219.
23. Matheisa, C., Wohnsiedlera, S., Ospalda, F., & Cristofanib, E. (2014). Terahertz FMCW inspection of GFRP composites: Comparison with conventional NDT techniques and enhanced defect detection capability through. In *Microwave conference* (pp. 1–4).
24. Yang, R., He, Y., & Zhang, H. (2016). Progress and trends in nondestructive testing and evaluation for wind turbine composite blade. *Renewable and Sustainable Energy Reviews, 60,* 1225–1250.
25. Mittleman, D. M., Hunsche, S. & Nuss, M. C. (1997) T-ray tomography. *Optics Letters*, *22*(12), 905–906
26. Lopato, P. (2017). Double-sided terahertz imaging of multilayered glass fiber-reinforced polymer. *Applied Sciences, 7*(7), 661–675.
27. Amolins, K., & Zhang, P. (2007). Wavelet based image fusion techniques—An introduction, review and comparison. *ISPRS Journal of Photogrammetry, 62*(4), 249–263.

Jie Wang received the B.S. degree in electrical engineering from Jilin University, Changchun, China, in 2017. She is currently pursuing the M. S. degree in instrument science and electrical engineering from Jilin University. Her main interests are terahertz imaging algorithm and detection of defects in composite materials.

Jin Zhang is currently a stuff member in the College of Instrumentation and Electrical Engineering, Jilin University. She received the B.S. degree and M.S. degree in Computer Science from Northeast Normal University, in 2008 and 2011, respectively. She received the Ph.D. degree in Measurement Technology and Instrument from Jilin University, in 2016. Her research interest is mainly focused on THz imagingtechnologies and nondestructive testing.

Tianying Chang received the M.S. and Ph.D. degrees in control science and engineering from Shandong University, Jinan, in 2009. From 2007 to 2008, she worked as joint PhD candidate at Stevens Institute of Technology (USA). After graduation, she was a lecturer in Shandong University at Weihai, and then went to Polytechnic Institute of New York University in America as a postdoctoral research associate. Now she is an associate professor in Jilin University, China and her research efforts have been con-

centrated in the areas of optical fiber sensor, THz system, and nano-optics.

Hong-Liang Cui received M.S. and Ph.D. degree in physical engineering from Stevens Institute of Technology at New Jersey, America, in 1987. He received Ph.D. degree in applied physics from New York University, New York, America, in 2011. From 1987 to 1990, he was a lecturer in Stevens Institute of Technology. From 1990 to 1995, he was a assistant professor in Stevens Institute of Technology. In 1996, he received tenure. Now his research efforts have been concentrated in the areas of solid-state electronics/nanoelectronics, optical communications and sensing, electromagnetic wave propagation and interaction with matters such as chemical and bio-warfare agents, and see-through-wall sensing, and highperformance computing approach to modeling of physical devices and phenomena. Prof. Cui is chair of IEEE-Nano Conferences.